Identification of Vehicle Dynamics Model and Lever-arm for Arbitrarily Mounted Motion Sensor

Y. Hwang, Y. Jeong, I.Kweon, *Senior Member, IEEE* and S.B.Choi, *Member, IEEE*

***Abstract*—This paper presents a novel identification method for vehicle dynamics model and sensor lever-arm using the motion measurements from sensors mounted on arbitrary positions. Since known methods for vehicle model parameter identification and sensor lever-arm estimation have been cross-referencing the results from each other, a simple conjugation of two methods cannot solve the identification of model parameter and lever-arm concurrently. A modified single track model with normalized tire stiffness is formulated to decouple the lever-arm effect from the vehicle's dynamics states. The identification scheme is conducted through an unscented Kalman filter by fusing the modified model with inertial and velocity measurements from the sensor. We demonstrate the efficacy of identification performance of the proposed method in simulations and real-vehicle experiments. The identified model accomplished the accuracy within 5% error for geometrical parameters and 10% error for tire stiffness over various experimental conditions and confirms the feasibility of utilizing motion estimation devices in vehicle dynamics and vice versa.**

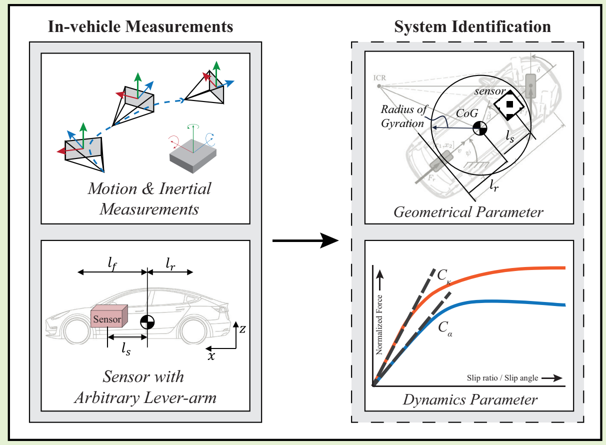

***Index Terms*—Motion estimation, Sensor fusion, System identification, Vehicle dynamics, Extrinsic calibration**

I. Introduction

RESEARCHES on the advanced driver assistance system(ADAS) and self-driving cars have been gaining momentum under the emerging attention of the automotive industry and academia. Over the last decade, numerous mass-produced vehicles are produced with state-of-the-art sensor systems, such as lidar, radar, camera, or global navigation satellite system(GNSS) [1]. This innovation of the sensor systems not only offers the advantage of recognizing the surrounding driving scenes but the capability of potential enhancement on the vehicle model and state estimation for the active safety control on various conditions.

This work was supported by a grant (20TLRP-C152478-02) from the Transportation and Logistics Research Program funded by the Ministry of Land, Infrastructure and Transport(MOLIT) of the Korean government and the Korea Agency for Infrastructure Technology Advancement(KAIA), the National Research Foundation of Korea(NRF) grant(No. 2020R1A2B5B01001531) funded by the Korea government(MSIP) and The Technology Innovation Program (20014983, Development of autonomous chassis platform for a modular vehicle) funded By the Ministry of Trade, Industry Energy(MOTIE, Korea)

Y. Hwang is with the Department of Mechanical Engineering, Korea Advanced Institute of Science and Technology(KAIST), Daejeon 34141 Republic of Korea (e-mail: yoonjinh@kaist.ac.kr).

Y. Jeong is with the Robotics Program, Korea Advanced Institute of Science and Technology(KAIST), Daejeon 34141 Republic of Korea (e-mail: yongseop@kaist.ac.kr).

I. Kweon is with the Department of Electrical Engineering, Korea Advanced Institute of Science and Technology(KAIST), Daejeon 34141 Republic of Korea (e-mail: iskweon77@kaist.ac.kr).

S. B. Choi is with the Department of Mechanical Engineering, Korea Advanced Institute of Science and Technology(KAIST), Daejeon 34141 Republic of Korea (e-mail: sbchoi@kaist.ac.kr).

The sensor systems for ADAS not only provide the relative motions of moving objects by detecting distinguishable features from the given scenes but also estimate the position and motion of ego-vehicle by referencing stationary features in the surrounding environment. In order to accomplish precise localization and accurate state estimation through external sensing, several studies based on various types of sensors have been introduced. Inertial navigation system with GNSS aiding provides a capability of vehicle state estimation [2]–[4], and also achieves the centimeter-level of positioning accuracy with real-time kinematics(RTK) technology [5], [6]. Furthermore, based on pose optimization approaches, the motion estimation techniques have been introduced using ADAS sensors, such as camera [7]–[10], lidar [11] or radar [12], [13] and being widely applied in GNSS-denied environments including indoor positioning.

The motion estimation methods mentioned above are only relying on their own measurement characteristics, whereas the actual motion of land vehicles follows the vehicle dynamics model strictly constrained on the ground. Consequently, by combining the dynamic motion constraints from the vehicle model, the comprehensive motion estimation gives benefits for improved performance and robustness [14]–[18]. Moreover, the motion estimation provides attitude and velocity information of the vehicle as well as position information, which enables itself as a state estimator for vehicle dynamics and control applications. The vehicle dynamics state estimation methods based on external environment sensing, such as vision [19], [20] or lidar [21], have been proposed and validated that the additional sensor modality can effectively reduce the drift and error in sideslip estimation.

However, there exist preliminary requirements when integrating vehicle dynamics equations with motion estimation techniques. First, in practice, the mounting position of sensors in consumer vehicles usually does not coincide with the center-of-gravity(CoG) of vehicles due to technical reasons. The distance between the sensor body to vehicle CoG, called sensor lever-arm, induces addictive quantities on the raw measurement and needs to be compensated when merging the measurement with the vehicle dynamics model [22]. Second, the model-based integration requires an adequate vehicle dynamics model that is built upon several physical parameters which are hard to be directly measured.

For the identification of sensor lever-arm which is off-center mounted in the vehicle body, several estimation methods have been proposed. The non-holonomic constraint(NHC) assumption is a conventional way used to eliminate the effect of the lever-arm. It assumes that there is no slip occurs on the rear axle, thus the lateral and vertical velocities at the rear axle are considered as zero. Then the distance between the rear axle and sensor position can be determined using the kinematic constraints on velocity measurements [23]–[25]. However, adopting NHC into the vehicle model parameter identification can lead to erroneous results, since the vehicle dynamics model is derived from the tire force generated by slip, which directly conflicts with NHC assumption [26].

As for the dynamics model, various techniques have been applied to obtain the vehicle parameters [27]. The longitudinal tire stiffness can be calculated from the wheel dynamics [28], [29], and the lateral tire stiffness also can be estimated based on the relationship between the sideslip angle and tire force [30]–[33]. For the vehicle inertial parameters, such as mass, moment of inertia, and axle distance from CoG, recursive system identification methods based on the single track model are introduced [34]–[36], but those parameter identification methods are formulated with the motion and inertial measurements acting on vehicle CoG, which is the target of identification itself.

Alternatively, to overcome the limitations above, a dual Kalman filter approach considering sensor lever-arm for vehicle motion state estimation was introduced [37], [38]. This method establishes a Kalman filter to obtain an indirect estimation of virtual measurements at vehicle CoG, while another Kalman filter estimates the vehicle model parameter using the virtual measurement, in parallel. However, this method also has the prerequisite that the distance between IMU and the front axle of the vehicle should be configurated with respect to the vehicle body frame when generating the virtual measurement. Thus, there is still a remaining issue in the implementation of an integrated state estimator for the unknown vehicle model and sensor position.

Taking the above into account, those two requirements for the integration of the vehicle model and motion estimation need contradictory preliminaries in their identification strategy: Sensor to vehicle CoG lever-arm identification has a precise vehicle model as a prerequisite, whereas the vehicle dynamics parameter estimation has a mounting location of the sensor as a prerequisite. Accordingly, the fusion of various modalities with the dynamics model is mainly based on relative motion constraints with respect to each sensor [39], not being governed by the vehicle dynamics equations which dominate the motion of land vehicles.

In this paper, we introduce a novel method for simultaneous identification of vehicle dynamics parameters and sensor lever-arm for arbitrarily mounted motion sensors. The proposed method takes the inputs as yaw rate, acceleration, and velocity for longitudinal and lateral direction, measured on the sensor position, and also requires in-vehicle sensors including steering angle and odometer measurement. The identified model consists of the following fundamental vehicle dynamics parameters: normalized tire stiffness for longitudinal and lateral direction, radius of gyration of vehicle, longitudinal position of CoG and the corresponding sensor lever-arm. The identification process is constructed on a combination of longitudinal and lateral dynamics of vehicle with a linearized tire model, and how the dynamics states presented in the measurement under the lever-arm effect. As a result, a modified single track model with lever-arm compensation is formulated and integrated with sensor measurements via an unscented Kalman filter(UKF). The identification results for vehicle dynamics model parameters and sensor lever-arm are evaluated with numerical simulations and vehicle experiments.

II. Vehicle and Sensor Model

In this section, we introduce the equations of motion for the linearized vehicle dynamics model for both longitudinal and lateral motions, and the corresponding measurement influence due to the mounting position of motion sensors with respect to vehicle CoG.

Assuming the vehicle chassis as a rigid body, the Newton-Euler equations of motion for the vehicle on a plane become

$$F_x = m\dot{v}_x - mrv_y \tag{1}$$

$$F_y = m\dot{v}_y + mrv_x \tag{2}$$

$$M_z = \dot{r}I_z \tag{3}$$

When the lateral movement of the vehicle, v_y is relatively small compared to the forward velocity v_x, we can assume that

$$v_x = v\cos\beta \approx v \tag{4}$$

$$v_y = v\sin\beta \approx v\beta \tag{5}$$

where β is the sideslip angle, defined by $\beta \approx \frac{v_y}{v_x}$, and v is the planar speed of the vehicle. Then, the longitudinal and lateral forces acting on the vehicle can be represented in terms of β as follows.

$$F_x \approx m\dot{v} - mrv\beta \tag{6}$$

$$F_y \approx m\dot{v}\beta + mv(r + \dot{\beta}) \tag{7}$$

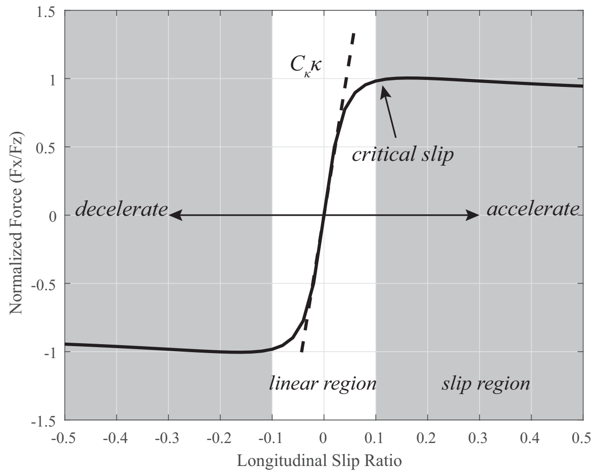

Fig. 1. Normalized longitudinal tire force with respect to tire slip ratio

When the aerodynamic effect is negligible, the only force acting on a vehicle is the friction between the ground and tires. Due to the highly nonlinear characteristics of tires, there are numerous parameters that affect the tire force. However, the tire force can be simplified with a linear coefficient when the contact surface to the ground is nearly in stick condition. In the following, we will describe the details of the vehicle dynamics model using the linear tire model, and how it manifests itself in the sensor measurement.

A. Longitudinal Dynamics

When a vehicle accelerates or decelerates, there are speed differences between tires and the ground speed developed. The longitudinal slip ratio of a tire, κ, is defined as

$$\kappa = \frac{R\omega_{wheel} - v_x}{v_x} \tag{8}$$

where R is the nominal radius of the tire, and ω_{wheel} is the angular velocity measured from vehicle's wheel speed sensor.

The longitudinal force between a tire and the ground depends on the vertical load F_z and the slip ratio κ. As shown in Fig. 1, the normalized force is proportional to the slip ratio in a small slip region and saturated when the slip ratio exceeds a certain slip ratio. Hence, in a mild driving maneuver, the longitudinal force (1) can be written as

$$F_{xi} = C_{\kappa i}(\kappa_i, F_{zi}) \cdot \kappa_i \tag{9}$$

$$C_{\kappa i} \approx C_\kappa F_{zi} \tag{10}$$

where C_κ is the normalized longitudinal stiffness of tires and the subscript i denotes the axle, front or rear, where equations acting on.

Considering that a vehicle commonly uses the same tires on all wheels, and moves on a uniform surface, the longitudinal forces acting on the front and rear axle can be derived with the vertical load and the slip ratio. The vertical load of each axle is determined by the position of CoG, and the dynamic load transfer due to the longitudinal acceleration,

$$F_{zf} = m(g\frac{l_r}{l} - a_x\frac{h}{l}) \tag{11}$$

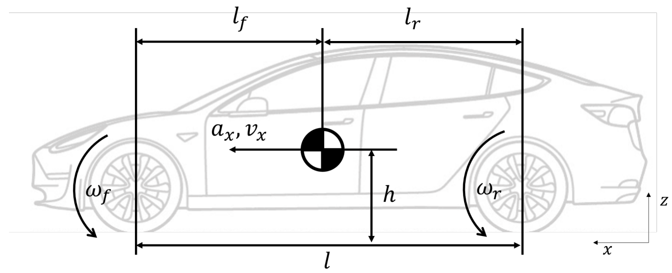

Fig. 2. Longitudinal vehicle model

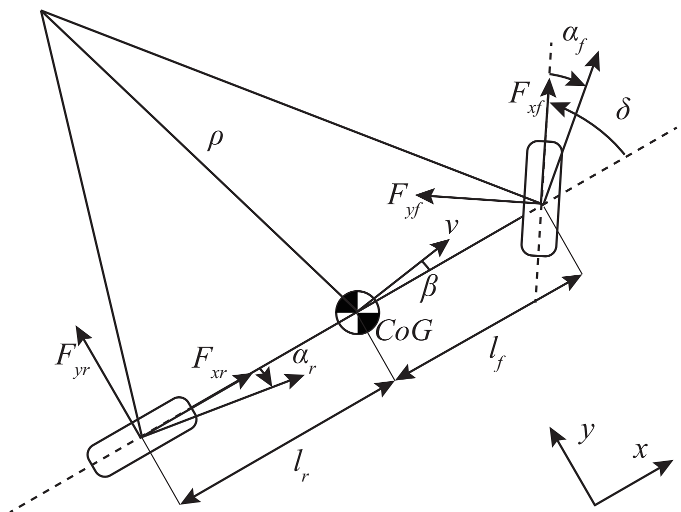

Fig. 3. Single Track Model Geometry

$$F_{zr} = m(g\frac{l_f}{l} + a_x\frac{h}{l}) \tag{12}$$

where g is the gravitational constant, l refers to the wheelbase length, l_r and l_f refer to the distances from CoG to front and rear axles respectively, and h refers to the height of CoG.

Combining (9)-(12), the longitudinal force generated by the front and rear tires becomes the function of the longitudinal slip ratio κ with the nominal longitudinal tire stiffness C_κ.

$$F_{xf} = mC_\kappa\frac{(gl_r - a_x h)}{l}\kappa_f \tag{13}$$

$$F_{xr} = mC_\kappa\frac{(gl_f + a_x h)}{l}\kappa_r \tag{14}$$

Note that the longitudinal forces, (13) and (14), refer to the forces acting on each axle, not per tire, hence we use the average of κ of two tires on the same axle.

B. Lateral Dynamics

The single track model(also known as "bicycle model") assumes that the lateral dynamics of a vehicle can be described by the equivalent single tire per axle, while the roll dynamics including the lateral load transfer is neglected. Fig. 3 shows the geometry of the single track model when the vehicle turns with an instant turning radius ρ.

From the equations of motion of the vehicle, (1)-(3), the single track model approximation of vehicle dynamics can be derived. We can rewrite (2) and (3) in terms of the front and rear tire force F_{yf} and F_{yr} as follows,

$$F_y = F_{yf} + F_{yr} \tag{15}$$
$$M_z = l_f F_{yf} - l_r F_{yr} \tag{16}$$

In the same manner as the previous section, it is known that the lateral force of tire is proportional to the sideslip angle of tire α, with the lateral tire stiffness(also known as "cornering stiffness"), $C_{\alpha i}$,

$$F_{yi} = -C_{\alpha i}(\alpha_i, F_{zi}) \cdot \alpha_i \tag{17}$$

where the sideslip angle of each tire α_i can be calculated by

$$\alpha_f = \beta + l_f \frac{r}{v_x} - \delta \tag{18}$$
$$\alpha_r = \beta - l_r \frac{r}{v_x} \tag{19}$$

with the given front steering angle δ.

Substituting (15)-(19) into (2)-(3), the single track model for the sideslip β and yaw rate r is derived as below.

$$\begin{bmatrix} \dot{\beta} \\ \dot{r} \end{bmatrix} = \begin{bmatrix} -\frac{C_{\alpha f}+C_{\alpha r}}{m v_x} & -\frac{l_f C_{\alpha f} - l_r C_{\alpha r}}{m v_x^2} - 1 \\ -\frac{l_f C_{\alpha f} - l_r C_{\alpha r}}{I_z} & -\frac{l_f^2 C_{\alpha f} + l_r^2 C_{\alpha r}}{I_z v_x} \end{bmatrix} \begin{bmatrix} \beta \\ r \end{bmatrix} + \begin{bmatrix} \frac{C_{\alpha f}}{m v_x} \\ \frac{l_f C_{\alpha f}}{I_z} \end{bmatrix} \delta \tag{20}$$

In general, the lateral tire stiffness can be approximated as a constant when the effect of lateral load transfer is negligible.

$$C_{\alpha f} = C_\alpha F_{zf} \tag{21}$$
$$C_{\alpha r} = C_\alpha F_{zr} \tag{22}$$

where C_α is the normalized lateral tire stiffness, which remains constant locally on the homogeneous road surface. Then, substituting lateral tire stiffness with normalized lateral stiffness and longitudinal weight transfer model, the lateral tire force can be established as follows,

$$F_{yf} = -mC_\alpha \frac{(g l_r - a_x h)}{l}(\beta + r l_f - \delta) \tag{23}$$
$$F_{yr} = -mC_\alpha \frac{(g l_f + a_x h)}{l}(\beta - r l_r) \tag{24}$$

Assuming that the magnitude of sideslip angle, β, is not huge, the longitudinal velocity of the vehicle can be approximated with the ground speed, and then the single track model in (20) is represented with the normalized tire stiffness as follows,

$$\begin{aligned} \begin{bmatrix} \dot{\beta} \\ \dot{r} \end{bmatrix} &= \begin{bmatrix} -\frac{C_\alpha}{v} g & \frac{C_\alpha}{v^2} a_x h - 1 \\ \frac{1}{k^2} C_\alpha a_x h & -\frac{1}{k^2} \frac{C_\alpha (g l_f l_r - (l_f - l_r) a_x h)}{v} \end{bmatrix} \begin{bmatrix} \beta \\ r \end{bmatrix} \\ &+ \begin{bmatrix} \frac{C_\alpha}{vl}(g l_r - a_x h) \\ \frac{1}{k^2} \frac{C_\alpha l_f}{l}(g l_r - a_x h) \end{bmatrix} \delta \end{aligned} \tag{25}$$

where $\bar{k}$ is the radius of gyration, defined as follows.

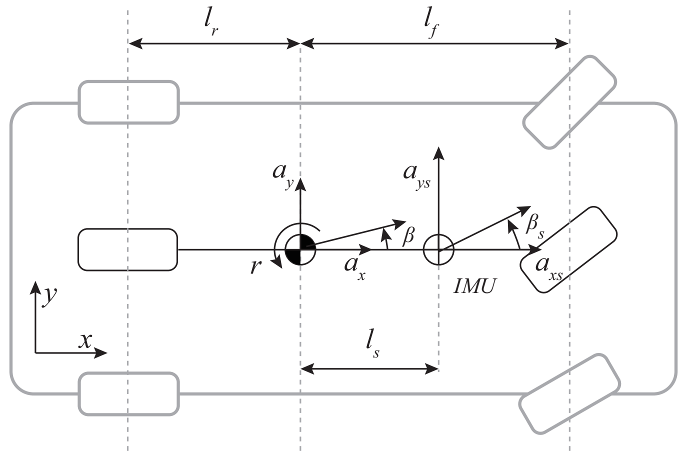

Fig. 4. Discrepancy between sensor mount position and vehicle CoG

C. Vehicle Dynamics Model with Sensor Lever-arm

The vehicle dynamics equations given in the previous sections are formulated on the assumption that the position of sensing devices is coincident with vehicle CoG. For the sensor mounted on the remote position, the measured values differ from that measured on vehicle CoG [40]. Hence a direct feed of sensor measurement to the original dynamics equations becomes no longer valid and a modified dynamics model that compensates kinematic relationships between vehicle CoG and sensor measurement is required.

The acceleration of the vehicle CoG can be expressed by sum of tire forces.

$$m a_x = F_{xf} + F_{xr} - F_{yf}\delta \tag{26}$$
$$m a_y = F_{yf} + F_{yr} \tag{27}$$

Note that the longitudinal acceleration contains F_{yf}, whereas the lateral acceleration does not. Since this research assumes the moderate driving maneuver, harsh braking or acceleration on a curved road is not considered. However, even the vehicle moves with a stationary turn, the lateral force of the front tire can be applied along longitudinal direction under tight turns.

The sensor measurement is influenced by the lever-arm effect, induced by the motion of the vehicle. With the unknown lever-arm distance, l_s, between the sensor and vehicle CoG, the inertial measurements from the sensor becomes

$$r_s = r \tag{28}$$
$$a_{x,s} = a_x - l_s r^2 + g\theta \tag{29}$$
$$a_{y,s} = a_y + l_s \dot{r} + g\phi \tag{30}$$

where the subscript s is for the quantity on sensor position, and θ and ϕ are vehicle pitch and roll angle, respectively. The corresponding measurement of the sideslip angle on the sensor position, β_s, is also added by an extra component from the sensor lever-arm.

$$\beta_s = \beta + l_s \frac{r}{v} \tag{31}$$

Combining the linear tire force models denoted in previous sections, (13)-(14) and (23)-(24), and the sensor measurement models, (26)-(31), the acceleration measurements from the sensor can be represented with tire stiffness and slip:

$$\begin{aligned} a_{x,s} =& C_\kappa\left(\frac{gl_r - a_x h}{l}\kappa_f + \frac{gl_f + a_x h}{l}\kappa_r\right) \\ & - C_\alpha \frac{gl_r - a_x h}{l}\alpha_f \delta + rv\left(\beta_s - l_s \frac{r}{v}\right) + g\theta \end{aligned} \tag{32}$$

$$a_{y,s} = C_\alpha \left(-g\beta_s + (gl_s + a_x h)\frac{r}{v} + (gl_r - a_x h)\frac{\delta}{l}\right) + g\phi \tag{33}$$

Also the single track model is modified in terms of the sensor measurements, including lever-arm effect.

$$\begin{aligned} \begin{bmatrix} \dot\beta_s \\ \dot r_s \end{bmatrix} =& \begin{bmatrix} -\frac{C_\alpha}{v} g & \frac{C_\alpha}{v^2} a_x h - 1 \\ \frac{1}{\bar k^2} C_\alpha a_x h & -\frac{1}{\bar k^2}\frac{C_\alpha (g l_f l_r - (l_f - l_r) a_x h)}{v} \end{bmatrix} \begin{bmatrix} \beta_s - l_s \frac{r}{v} \\ r \end{bmatrix} \\ & + \begin{bmatrix} \frac{C_\alpha}{vl}(gl_r - a_x h) \\ \frac{1}{\bar k^2}\frac{C_\alpha l_f}{l}(gl_r - a_x h) \end{bmatrix} \delta + \begin{bmatrix} \dot r \frac{l_s}{v} \\ 0 \end{bmatrix} \end{aligned} \tag{34}$$

The derivative of sideslip angle, $\dot\beta_s$, can be formulated based on the kinematic relationship from the measurement itself without consideration of vehicle motion:

$$\dot\beta_{s,kin} = \frac{a_{y,s} - g\phi}{v} - r \tag{35}$$

Although the sensor has the capability to measure the sideslip angle directly, the system becomes highly sensitive when it depends on velocity measurements which can suffer external disturbances such as GNSS signal outage. Hence, alternatively, the kinematic model, (35), is adopted to obtain the time derivative of sideslip angle.

III. Parameter Identification Filter

The vehicle model provided in the previous section contains vehicle-specific parameters such as the tire stiffness, position of CoG, and sensor lever-arm, which are normally hard to determine. In order to achieve reconstructing the vehicle dynamics model, and validate the potential capability for complementary performance enhancement through sensor fusion from additionally mounted sensors, an online parameter identification filter is suggested.

As mentioned briefly in the previous section, identification approaches based on the steady-state response of the single track model would not be applicable for the system that contains off-centered measurement. From the basic form of the single track model, (20), it can be easily found that a simple replacement of dynamics states with compensated states, (28)-(31), leaves CoG position and sensor lever-arm as fully coupled.

In order to identify indistinguishable states in the single track model, a simultaneous identification process of the longitudinal and lateral dynamics of the vehicle is established. The proposed method utilizes the inertial and motion estimation results from sensors mounted on a land vehicle and provides the relative location of motion sensors from vehicle CoG, as well as, corresponding vehicle dynamics model in the linear slip region.

The identification process of vehicle model parameters is based on the Kalman filter, which is widely used to obtain the optimal solution for rank deficient systems. Originally, the Kalman filter is constructed for linear-time-invariant systems, thus the prediction and correction model need to be in the form of linear combinations of states.

For non-linear systems, an extended version of the Kalman filter is developed, which performs a linearization of nonlinear models around recently estimated states for each step. The EKF approximates the system dynamics as the first-order Taylor approximation, and the probability density as a Gaussian distribution, which requires the numerical calculation of Jacobian matrices at every update.

As the degraded performance of EKF of a system with the probability distribution of a random vector, the UKF was proposed [41], [42]. The UKF is based on the unscented transform, which gives the accuracy up to a second-order Taylor approximation, whereas the computational effort has the same order $O(n^3)$ as that of the EKF. Additionally, the estimation architecture of the UKF does not require the derivatives, which brings convenience to the implementation of practical systems.

In the rest of this section, the identifiability analysis and the UKF formulation for the vehicle model parameter estimation will be demonstrated.

A. System Identifiability

The unknown vehicle model parameters, l_r, l_s, C_α, C_κ, and $\bar k$, need to be determined to comprise the vehicle dynamics model given in the previous section. The state vector and available measurements used to establish identification filter are as follows, respectively,

$$\hat{\mathbf{x}} = \begin{bmatrix} \hat l_r & \hat C_\kappa & \hat C_\alpha & \hat l_s & \hat{\bar k} \end{bmatrix}^\mathsf{T} \tag{36}$$

$$\mathbf{z} = \begin{bmatrix} \dot\beta_{s,kin} & \dot r & a_{x,s} & a_{y,s} \end{bmatrix}^\mathsf{T} \tag{37}$$

and the corresponding measurement model derived with the vehicle dynamics model, (32)-(34), can be represented in terms of the filter state,

$$\begin{aligned} \hat{\mathbf{z}} =& h(\hat{\mathbf{x}}, \mathbf{u}) \\ =& \begin{bmatrix} -\frac{g}{v}\hat C_\alpha \left(\beta_s - \hat l_s \frac{r}{v}\right) + \frac{a_x h}{v^2}\hat C_\alpha r - r + \frac{g\hat l_r - a_x h}{vl}\hat C_\alpha \delta + \dot r \frac{\hat l_s}{v} \\ \frac{1}{\bar k^2}\left(a_x h\left(\beta_s - \hat l_s \frac{r}{v}\right) - \left(\hat l_f \hat l_r g - \left(\hat l_f - \hat l_r\right) a_x h\right)\frac{r}{v} + \hat l_f\left(g\hat l_r - a_x h\right)\frac{\delta}{l}\right) \\ \hat C_\kappa\left(\frac{g\hat l_r - a_x h}{l}\kappa_f + \frac{g\hat l_f + a_x h}{l}\kappa_r\right) - \hat C_\alpha \frac{g\hat l_r - a_x h}{l}\alpha_f \delta + rv\left(\beta_s - \hat l_s \frac{r}{v}\right) + g\theta \\ \hat C_\alpha\left(-g\beta_s + (g\hat l_s + a_x h)\frac{r}{v} + (g\hat l_r - a_x h)\frac{\delta}{l}\right) + g\phi + \dot r \hat l_s \end{bmatrix} \end{aligned} \tag{38}$$

where the hat operator denotes a estimated value.

The structural identifiability for the given system is evaluated by investigating the identifiability matrix, $\mathcal{O}_I(\mathbf{x}, \mathbf{u})$ defined by

$$\mathcal{O}_I = \begin{pmatrix} \frac{\partial}{\partial \mathbf{x}} h(\mathbf{x}, \mathbf{u}) \\ \frac{\partial}{\partial \mathbf{x}} \mathcal{L} h(\mathbf{x}, \mathbf{u}) \\ \vdots \\ \frac{\partial}{\partial \mathbf{x}} \mathcal{L}^{n-1} h(\mathbf{x}, \mathbf{u}) \end{pmatrix} \tag{39}$$

where the operator, $\mathcal{L}^i$, denotes the ith order extended Lie derivative defined by

$$\mathcal{L}^i h(\mathbf{x}, \mathbf{u}) = \sum_{j=0}^{\infty} \frac{\partial \mathcal{L}^{i-1} h(\mathbf{x}, \mathbf{u})}{\partial \mathbf{u}^{(j)}} \mathbf{u}^{(j+1)} \tag{40}$$

where $\mathbf{u}^{(j)}$ is the jth time derivative of u [43]. If the system with $n_{\mathbf{x}}$ independent states satisfies $\mathbf{rank}(\mathcal{O}_I(\mathbf{x}, \mathbf{u})) = n_{\mathbf{x}}$, then the model is locally structurally identifiable [44], [45].

Although the first order Jacobian matrix for the given system, $\frac{\partial}{\partial \mathbf{x}} h(\mathbf{x}, \mathbf{u})$, has the rank deficiency, the extended Lie derivative of $h(\mathbf{x}, \mathbf{u})$ implies full column rank of $\mathcal{O}_I$, with the consideration of the system input $\mathbf{u} = \begin{bmatrix} \beta_s & r & \delta \end{bmatrix}$. It should be noted that the system only has full rank with non-zero excitation of the lateral movement, hence the update process should be limited to the longitudinal parameters when the vehicle moves in a straight trajectory.

B. UKF Formulation

The parameter estimation proposed in this research is performed by the UKF. The key difference between the UKF and the EKF is the approximation method for nonlinear models. The UKF linearizes the system by the statistical linearization method, based on the unscented transform. This method approximates the system with a linear regression over $2n + 1$ point, chosen by the prior distribution of the states. These points are called the sigma points, given by the following transformation

$$\chi_i = \begin{cases} \hat{\mathbf{x}}_{k|k-1} & \text{if } i = 0 \\ \hat{\mathbf{x}}_{k|k-1} + \sqrt{(n+\lambda)\Sigma_{k|k-1}}_i & \text{if } 0 < i \leq n \\ \hat{\mathbf{x}}_{k|k-1} - \sqrt{(n+\lambda)\Sigma_{k|k-1}}_i & \text{if } n < i \leq 2n \end{cases} \tag{41}$$

where χ, Σ, and λ denote the sigma points, prior states covariance, and a scaling parameter, given by $\lambda = a^2(n+k) - n$ with tuning parameters a and k, which determine the spread of the sigma points. The subscript $i|j$ denotes that the estimated parameter in ith step using the information of jth step.

The corresponding weights for each point are

$$\begin{aligned} \mathcal{W}_i^c &= \begin{cases} \frac{\lambda}{n+\lambda} + (1 - a^2 + b) & \text{if } i = 0 \\ \frac{1}{2(n+\lambda)} & \text{if } i \neq 0 \end{cases} \\ \mathcal{W}_i^m &= \begin{cases} \frac{\lambda}{n+\lambda} & \text{if } i = 0 \\ \frac{1}{2(n+\lambda)} & \text{if } i \neq 0 \end{cases} \end{aligned} \tag{42}$$

where $\mathcal{W}_i^c$ and $\mathcal{W}_i^m$ are weights for the covariance and mean calculation, respectively.

The average measurement, $\hat{z}$ is obtained according to the measurement model, (38), over the sigma points:

$$\mathcal{Z}_i = h(\chi_i) \tag{43}$$

$$\hat{z} = \sum_{i=0}^{2n} \mathcal{W}_i^m \mathcal{Z}_i \tag{44}$$

Similarly, the error and state covariance are propagated as below

$$S = \sum_{i=0}^{2n} \mathcal{W}_i^c (\mathcal{Z}_i - \hat{z})(\mathcal{Z}_i - \hat{z})^{\mathsf{T}} + R \tag{45}$$

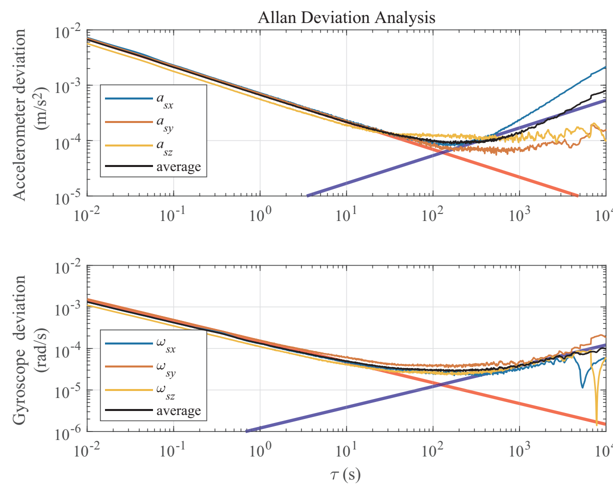

Fig. 5. Allan-variance characteristics of IMU(Xsens MTi-670g)

TABLE I
IMU NOISE AND BIAS CHARACTERISTICS

Xsens MTi-670G	Characteristics	Unit	Measured	Datasheet
Accelerometer	Noise density, σ_a	$\frac{m}{s^2}\frac{1}{\sqrt{Hz}}$	6.9e-4	5.9e-4
	Random walk, σ_{ba}	$\frac{m}{s^3}\frac{1}{\sqrt{Hz}}$	0.9e-5	N/A
	In-run bias stability	m/s^2	9.80e-6	9.81e-6
Gyroscope	Noise density, σ_g	$\frac{rad}{s}\frac{1}{\sqrt{Hz}}$	1.49e-4	1.22e-4
	Random walk, σ_{bg}	$\frac{rad}{s^2}\frac{1}{\sqrt{Hz}}$	2.0e-6	N/A
	In-run bias stability	deg/hr	6.21	8.0

$$\bar{\Sigma} = \sum_{i=0}^{2n} \mathcal{W}_i^c (\chi_i - \chi_0)(\mathcal{Z}_i - \hat{z}) + Q \tag{46}$$

where R and Q are the observation and process noise respectively.

The state correction is performed when a new set of measurement is available:

$$K = \bar{\Sigma} S^{-1} \tag{47}$$

$$\hat{\mathbf{x}}_{k|k} = \chi_0 + K(z - \hat{z}) \tag{48}$$

$$\Sigma_{k|k} = \bar{\Sigma} - K S K^{\mathsf{T}} \tag{49}$$

Since the vehicle parameters are time-invariant states, the prior state is not updated without the measurement correction, $\hat{\mathbf{x}}_{k|k-1} = \hat{\mathbf{x}}_{k-1|k-1}$.

Even though the vehicle parameters are constant properties, the process noise, Q, is added into the state covariance, Σ, for the purpose of maintaining the estimation performance against potential violations of model assumptions or environmental changes. Hence Q is adjusted as a tuning parameter, while the measurement noise covariance, R, can be determined by analyzing sensor characteristics through the Allan-variance method [46]. The standard deviation analysis for noise and random walk of IMU used in this research are represented in Fig. 5 and the result is summarized in Table I. According to the measured noise density of IMU, the measurement covariance for identification filter is derived and additional noise components are emulated in the simulation environment.

TABLE II
VEHICLE PARAMETERS USED IN SIMULATION

B-Class Sports Car	Parameter	Value	Unit
Vehicle mass	m	1140	kg
Moment of inertia	I_z	1320	kg m^2
Radius of gyration	$\bar{k}$	1.076	m
Wheelbase	l	2.33	m
Front axle distance	l_f	1.165	m
Rear axle distance	l_f	1.165	m
CoG Height	h	0.5	m
Nominal lateral tire stiffness $\sim |\alpha| < 0.1$	C_α	15	1/rad
Nominal longitudinal tire stiffness $\sim |\kappa| < 0.1$	C_κ	19	1/(slip ratio)
Sensor lever-arm	l_s	0.5	m

IV. SIMULATION AND EXPERIMENTAL RESULTS

The proposed identification method for vehicle model parameters and sensor mount position was evaluated by a numerical simulation. The aim of the simulation is to investigate the performance of the identification algorithm and explore the effect of the initial state and tuning parameters. Moreover, the simulation approach allows to validate the proposed method on various conditions, for example, modifying physical parameters of test vehicles, which is hard to be performed in the real situation for technical reasons. The simulation was performed on the CarSim, which is an industrial software for simulating and analyzing the vehicle dynamics. Also, the experimental validation was also established to evaluate the performance of the proposed method under unintended noise and assumption violations.

A. Simulation Results

All of the vehicle model parameters used for the simulation are summarized in Table II. The inertial and geometrical parameters are extracted from the vehicle model data, whereas the longitudinal and lateral tire stiffness are obtained using linear regression as shown in Fig. 6, since originally the stiffness is modeled as a function of the slip, vertical load, road surface friction, and elastic characteristics.

The simulations were made for various road shapes, but here the results of the representative scenario which contains several curves and straights are presented. The driving scenario is described in Fig. 7, considering the characteristics of real-world drivers in normal driving circumstances. According to the previous research for the driving pattern analysis [47], it had been shown that the majority of peak acceleration in a moderate driving scenario is 3-4$\mathrm{m/s^2}$. Therefore, the simulation driving maneuver is set to be limited to 3.5$\mathrm{m/s^2}$ for the longitudinal and lateral acceleration with the homogeneous road friction coefficient.

Fig. 8-9 shows the identified vehicle parameters with and without the correction of the sensor lever-arm effect. Without the simultaneous identification of the sensor lever-arm, the identified vehicle model converges to an incorrect direction to resolve the error from the lever-arm, l_s, with the own dynamics of the vehicle model itself, whereas the estimation results with the consideration of the lever-arm enhance the estimation performance of the vehicle parameters.

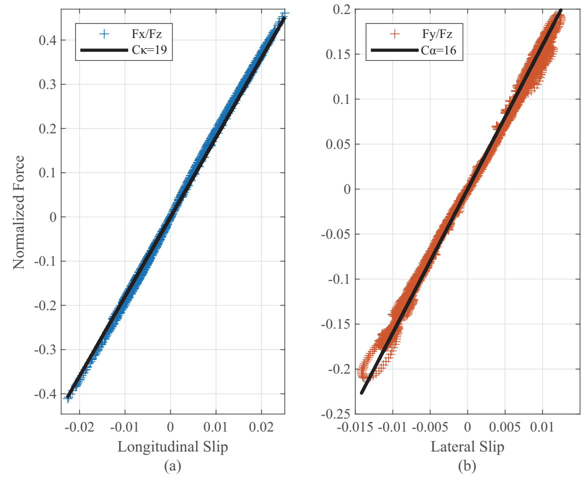

Fig. 6. Normalized tire force compared to linear model in the low-slip region: (a) Longitudinal normalized force versus $\boldsymbol{\kappa}$ (b) Lateral normalized force versus $\boldsymbol{\alpha}$

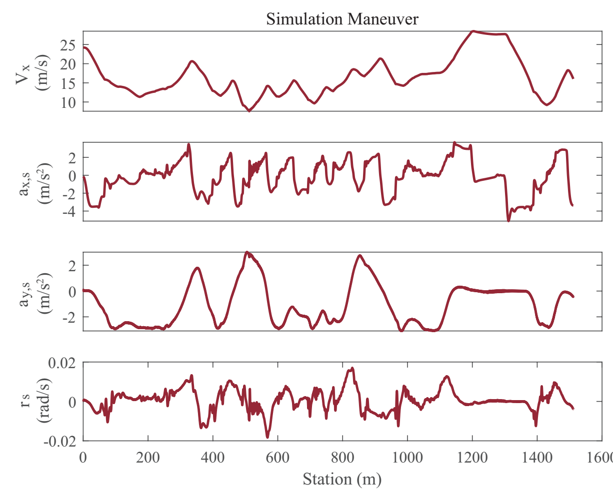

Fig. 7. Velocity and inertial measurements of the simulation scenario

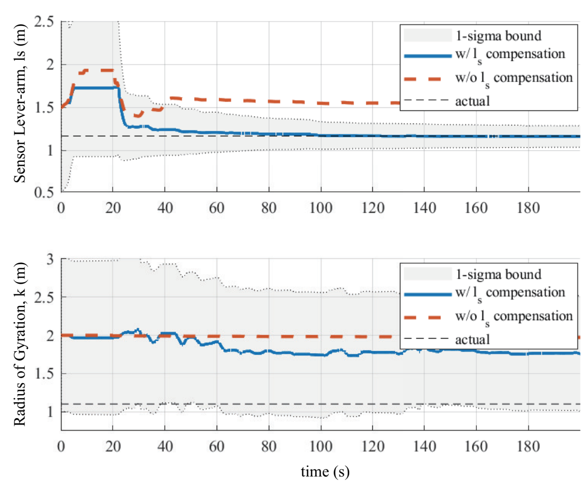

Fig. 8. Vehicle geometrical parameter identification result

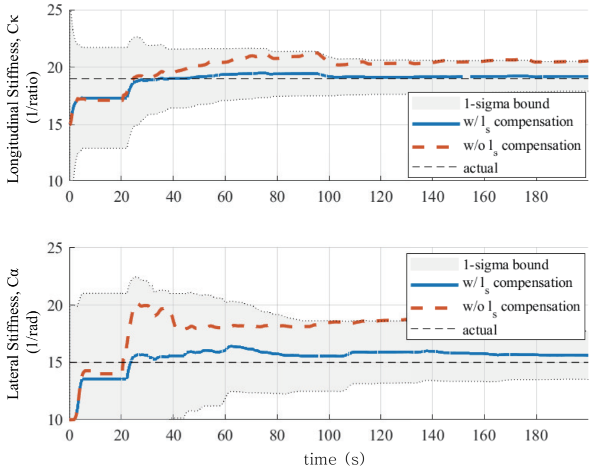

Fig. 9. Tire stiffness identification result

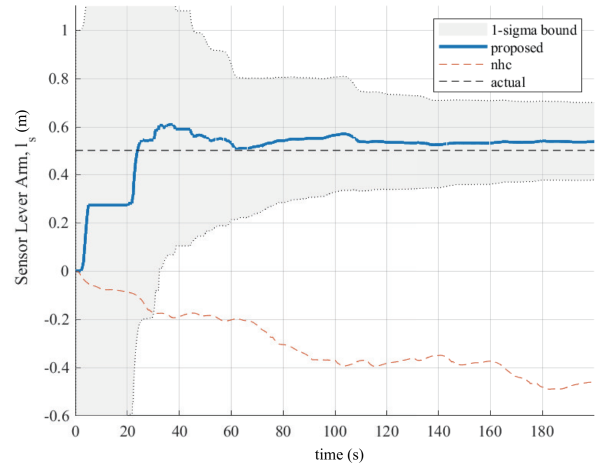

Fig. 11. Sensor to vehicle CoG Lever-arm estimation results

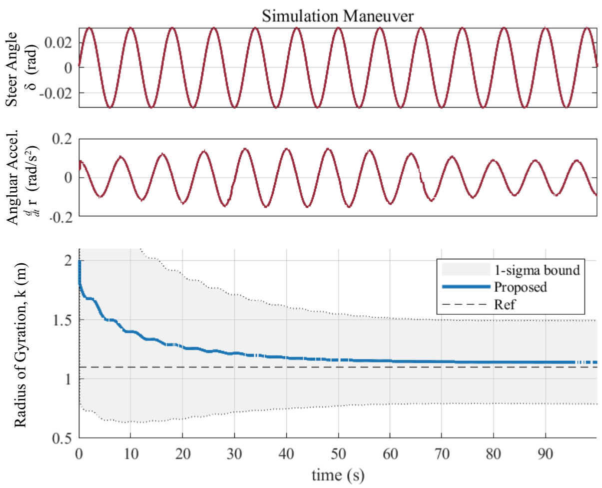

Fig. 10. Subsequent sine-wave steer scenario for the excitation signal of identifying radius of gyration.

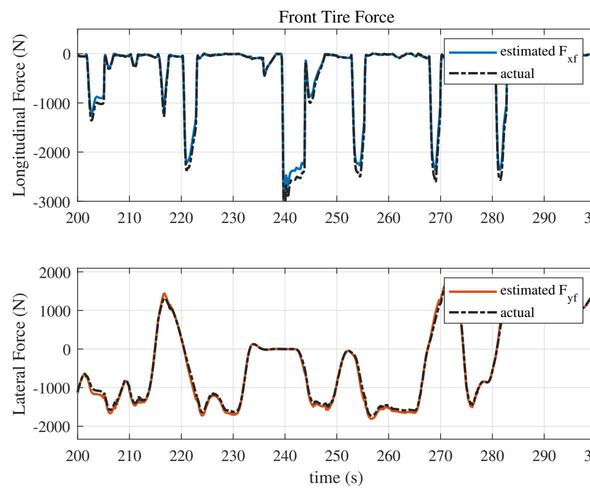

Fig. 12. Front tire forces obtained from the identified model

However, it is worth noting that the radius of gyration is not well converging to the actual value, while other estimations tend to converge to the actual model. Since the given driving maneuver in the simulation is hardly restricted, the excitation condition for the identification of $\bar{k}$ rarely occurs. Thus, we construct a subsequent scenario, which contains rotational excitation with sine-wave steer input. Fig. 10 shows the steer input and estimated $\bar{k}$ in additional maneuver.

The comparative result of the proposed method and NHC method for the sensor lever-arm estimation is presented in Fig. 11. It can be found that even the vehicle moves with low-level acceleration, the sideslip angle of the rear axle, α_r, violates the non-slip assumption, thus the estimation result of the NHC method obviously leads to a wrong value. Meanwhile, the proposed method provides an acceptable identification result based on the single track model. Fig. 12 and 13 show results of the longitudinal and lateral tire forces, for the front and rear axle respectively. The calculated tire forces are obtained by (13)-(14) and (23)-(24) using the identified vehicle model parameters. There can be found that the longitudinal force from the model shows emphasized error when the vehicle decelerating, whereas lateral tire force follows the actual value. It can be explained by the fact that we assumed that the suspension motion of the vehicle is negligible; therefore the tire force model does not contain the weight transfer due to angular motion, and as a result, the calculated longitudinal force has been biased to the rear axle when the peak deceleration is applied, while the summation of longitudinal tire force follows the actual value.

Reminding the main goal of the proposed identification method is providing information of vehicle motion constraint and sensor lever-arm for the integration of vehicle dynamics with state-of-the-art motion estimation technologies, a simple validation for the sideslip angle and yaw rate is conducted based on the identified vehicle model. The estimation follows an open-loop integration of the single track model, described in the previous section, with the estimated model parameters. As seen in Fig. 14, the identified model well represents the actual dynamics of the given condition. The sideslip angle reconstructed from the model achieves a reliable tracking

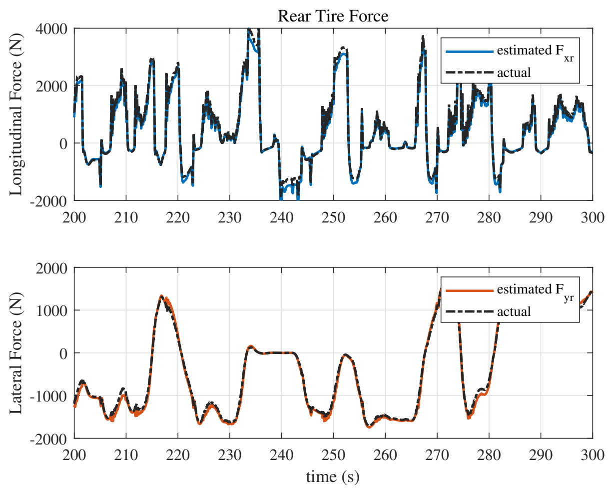

Fig. 13. Rear tire forces obtained from the identified model

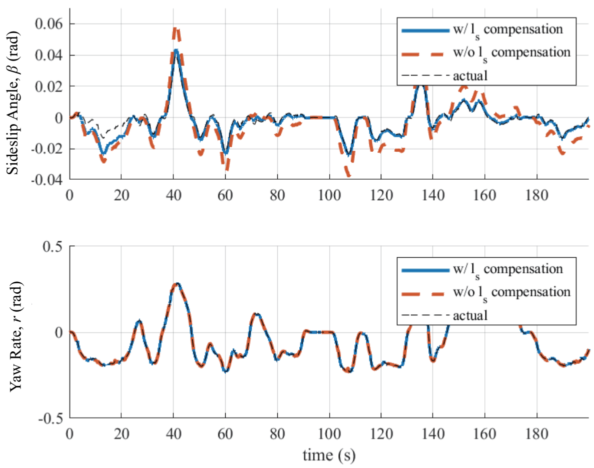

Fig. 14. Open-loop estimation results for sideslip angle and yaw rate with online identification of vehicle model parameters

performance of the actual β, even during the combined slip region. However, the yaw rate is not much varying from the actual value. The measurement model used in this research directly includes the yaw rate measurement, and the lever-arm effect does not implicate an interference on angular velocity measurements. As a result, the yaw rate given by the identified model shows less model sensitivity regardless of the accuracy of model parameters.

Additionally, the simulation was conducted both on the high and low surface friction condition, with the purpose of feasibility check for potential usage of proposed methods in the vehicle dynamics and control applications. The test consisted of two different surface conditions, $\mu = 1.0$ and $\mu = 0.6$, which are typical road friction coefficients for the dry pavement and wet pavement, respectively.

A comparison between the estimation results for different road friction is presented in Fig. 15(a) and Fig. 15(b). It can be seen the tire stiffness on the low friction surface has a lower value compared to that on the high friction surface. The tire behavior on different surfaces can be modeled by a

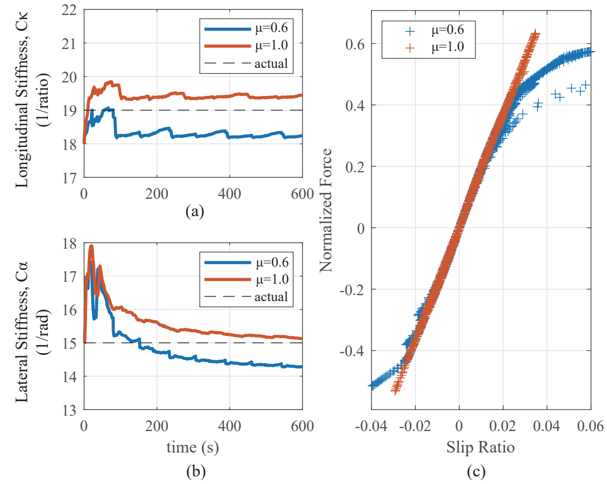

Fig. 15. Tire stiffness estimation on different types of road surface with same driving maneuver. (a)Longitudinal tire stiffness estimation. (b)Lateral tire stiffness estimation. (c)Force-slip curves for longitudinal normalized force.

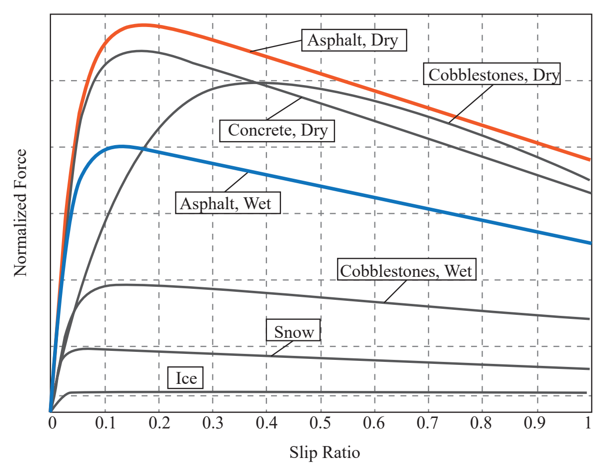

Fig. 16. Nominal curve for tire slip ratio and normalized force [48]; initial slopes for dry and wet pave road are almost same on linear region, whereas normalized force on wet surface(blue line) is saturated with smaller amount of slip than dry surface(orange line).

method called friction similarity, which predicts the effect of the degraded friction coefficient while maintaining the initial response in the small slip region [49]. This phenomenon is demonstrated in Fig. 15(c). The normalized force on the low friction surface has a similar slope to that on the high friction surface when the slip ratio is nearly zero. However, on the low friction surface, an excessive slip is required to generate the same amount of force, which causes saturation on the tire force. This result implies a potential necessity of the estimation criteria for switching the estimation strategy according to dynamics states for the real environment implementation.

Additional simulation scenarios to evaluate the identification performance under various model parameters also have been performed. Since the vehicle model parameters are hardly entangled with each other in single track model, the estimation performance of each parameter should not be affected while

TABLE III
IDENTIFICATION RESULTS FOR DIFFERENT VEHICLE MODELS IN SIMULATION (IDENTIFICATION ERROR)

Changed Parameter	Estimated Parameters and Error*				
	l_r (m)	l_s (m)	C_κ (1/ratio)	C_α (1/rad)	$\bar{k}$ (m)
Base Model (Table II)	1.171 (0.006)	0.467 (-0.033)	18.90 (-0.1)	16.28 (0.28)	1.069 (-0.008)
CoG Position ($l_r = 1.5$)	**1.487** (-0.013)	0.513 (0.013)	19.10 (0.1)	15.79 (-0.21)	1.087 (0.011)
Sensor Position ($l_s = -0.5$)	1.168 (0.002)	**-0.532** (-0.032)	18.83 (-0.17)	16.30 (0.30)	1.062 (-0.015)
Tire Stiffness ($C_\kappa = 26$, $C_\alpha = 19$)	1.196 (0.031)	0.444 (0.056)	**25.97** (-0.03)	**19.59** (0.59)	1.092 (0.016)
Radius of Gyr. ($\bar{k} = 1.4$)	1.171 (0.006)	0.493 (-0.007)	18.94 (-0.06)	15.83 (-0.17)	**1.389** (-0.011)

**stabilized result after 300s from initialization*

other parameters are changed. Table III shows the set of results of model identification for varying model parameters one by one. The result implies that the identification process of coupled parameters, such as CoG position and sensor lever-arm, is not affected by other parameters and shows consistent performance regardless of changes in the physical model.

B. Experimental Results

Although validation of the proposed algorithm was performed based on the numerical simulation, an experimental evaluation was conducted in order to secure the feasibility with unexpected or unmodeled disturbances. The test was performed with various types of dynamic maneuvers in the proving ground, to mitigate the propagation of motion estimation errors from external reasons such as road bank, inclination, or heterogeneous surface conditions. A passenger vehicle equipped with SINS(Xsens MTi-670G) was used in the experiments, and the available parameters for the experimental vehicle are as described in Table IV. The inertial parameters for the test vehicle were adopted by a kinematics and compliance(K&C) testing result for the same model, and the mass and longitudinal CoG position are obtained using a corner weight scale after the experimental equipment installed.

The test scenario is as described in Fig. 17. The maneuver consists of several acceleration and braking in the straight line,

TABLE IV
VEHICLE PARAMETERS USED IN EXPERIMENT

2016 Genesis G80 3.3 4WD	Parameter	Value	Unit
Vehicle mass	m	1998	kg
Moment of inertia*(Unloaded)*	I_z	4124	kg m^2
Radius of gyration*(Unloaded)*	$\bar{k}$	1.44	m
Wheelbase	l	3.01	m
Front axle distance	l_f	1.57	m
Rear axle distance	l_f	1.44	m
CoG Height*(Unloaded)*	h	0.52	m
Nominal lateral tire stiffness			
Typical value	C_α	10	1/(rad)
Nominal longitudinal tire stiffness			
Typical value	C_κ	20	1/(slip ratio)
Sensor lever-arm (P.G. Test)	l_s	-0.4	m
Sensor lever-arm (Road Test)	l_s	0.25	m

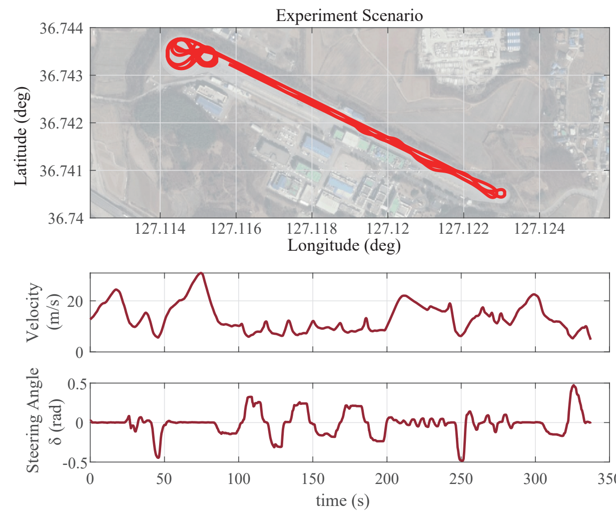

Fig. 17. Driving maneuver in the experiment

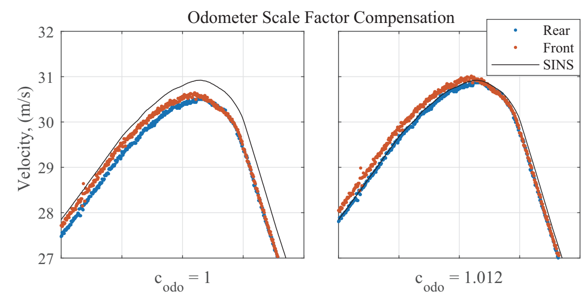

Fig. 18. Compensated odometer measurement with scale factor

and multiple loops of figure 8 shape turn which is intended to obtain the estimation result from a short period of driving fragments within a limited proving ground area.

However, unlike the simulation, the longitudinal slip ratio and the steering angle at the front wheels cannot be measured directly. The wheel speed measurements from in-vehicle odometers have a scale error depending on the effective radius of tires, and the steering system also has its own kinematics which is manifested in the nonlinear response of the wheel angle with respect to the rotation of the steering wheel. Thus, a simple regression process was performed to specify the coefficients of the odometer scale and steering ratio.

A comparative result for the odometer scale factor compensation is given in Fig. 18. Without the compensation, the calculated longitudinal slip denotes continuous negative slip. Thus, in this experiment, the odometer measurement is compensated with a coefficient of 1.012, and similarly, the steering ratio is set to be 13.8 within the range $(-90°, 90°)$.

Ideally, the measurement noise from the sensor is usually modeled as Gaussian noise, but the actual characteristic of sensor measurements may not follow zero-mean noise. Fig. 19 shows the raw measurement of sideslip from SINS and the filtered result. It can be found that there exists slowly varying error on the raw measurement which is mainly propagated from the heading attitude error, thus a bandpass filter is applied to the sideslip measurement to reduce the error from attitude estimation while maintaining the dynamic state information.

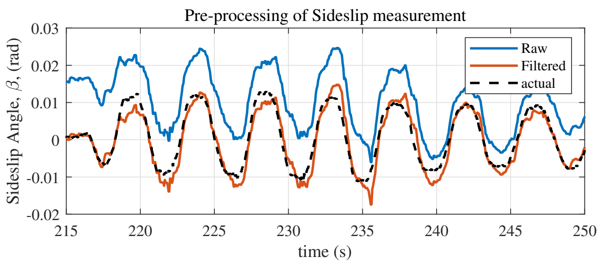

Fig. 19. Pre-processing of sideslip measurement to separate attitude error propagation: (blue) sideslip angle from SINS (red) bandpass filtered sideslip angle

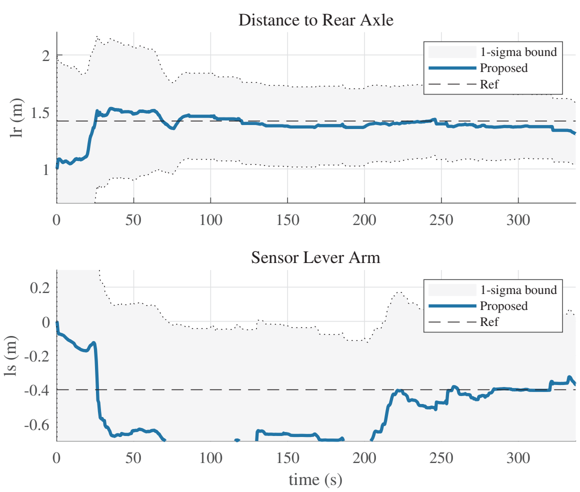

Fig. 20. Geometrical parameter identification results: (top) Vehicle CoG position identification (bottom) Sensor lever-arm identification

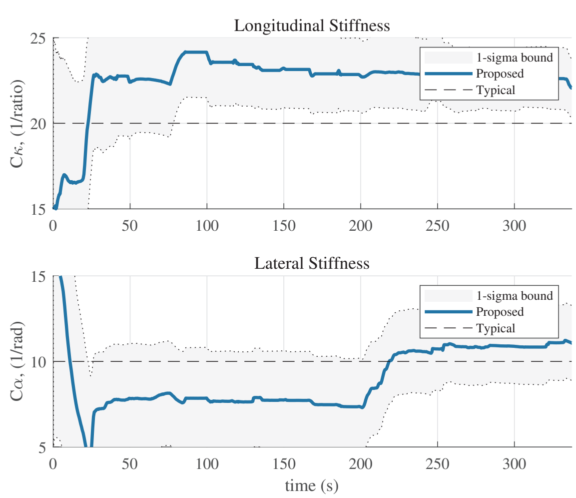

Fig. 21. Tire stiffness identification results: (top) Longitudinal tire stiffness (bottom) Lateral tire stiffness

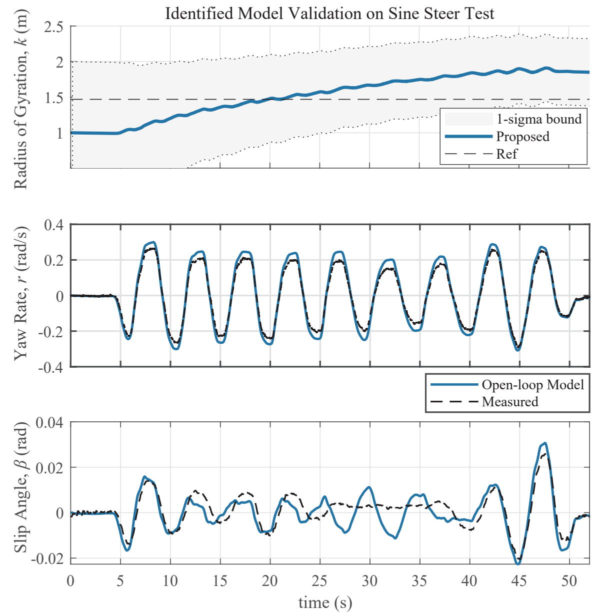

Fig. 22. Open-loop integration of identified model

The identification results for the experimental vehicle is presented in Fig. 20-21. The overall estimation results seem to follow the ground truth, whereas there exist fluctuations in the first half of the experimental maneuver. The fluctuations can be interpreted as due to the excessive steering angle in the corresponding section. As it can be found in Fig. 17, the maximum steering angle in the first half of the experimental scenario exceeds $360°$ which violates the assumption that the steering angle, δ, is small enough to approximate.

However, for the tire stiffness, the ground truth of the longitudinal and lateral stiffness is hard to be measured, while the identification results converge into the typical range for radial tires [50]. Thus, an indirect validation is established to ensure the performance of the proposed identification method by comparing the modeled dynamics states with the motion measurements.

Fig. 22 shows the open-loop estimation performance of the identified model. The yaw rate and the sideslip angle seem to be following the measured value in the acceptable range without additional sensor feedback. The sideslip model has an erroneous region, from $30s$ to $40s$, where braking is applied to the vehicle. Since the single track model assumes that the time derivative of longitudinal velocity is negligible, the model integration has its weakness with the speed change.

For the estimation result for the radius of gyration, $\bar{k}$ has been converged to a larger value than the unloaded moment of inertia. Although the moment of inertia of loaded vehicles cannot be measured, it is shown that the identified model well describes the motion of the vehicle, which is the primary purpose of the model identification.

In order to validate the identification performance on a normal driving situation, an additional experiment was performed on an urban street road. The vehicle parameters for the road test are set to be the same as the previous experiment, whereas

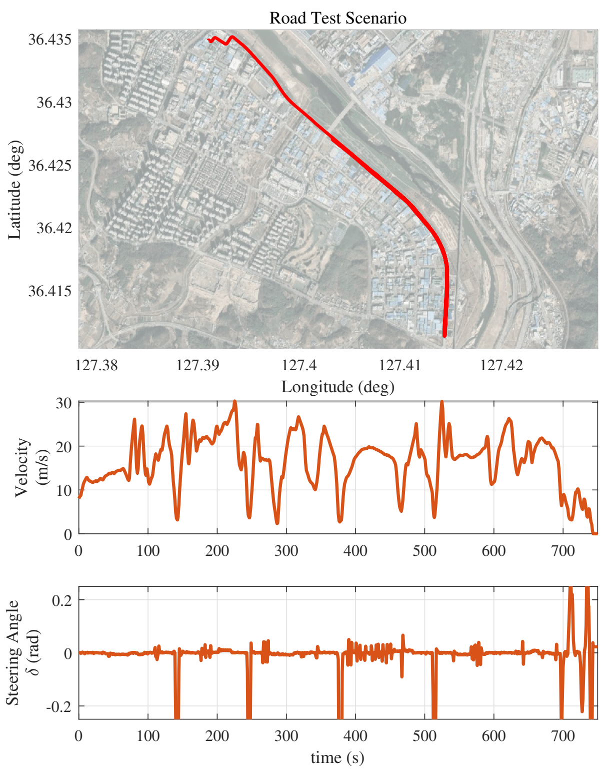

Fig. 23. Driving maneuver in the Road Test

the sensor mounting position is relocated as described in Table IV to demonstrate the consistency of model identification performance with arbitrary sensor position.

Unlike the proving ground experiments, driving in the street is strictly restricted to a few possible maneuvers, such as lane change, left or right turns. Fig. 23 shows the driving maneuver for the road test, and it can be found that the most of time is for straightforward driving with few lane changes and U-turns. Compared with the previous experimental maneuver, that leads to the overall process having less enough excitation state to update the model parameters and the identification results can be dominated by unintended disturbances. Furthermore, in a stop or low-speed condition, the measurement disturbances are emphasized since the definition of slip calculation includes longitudinal velocity as a denominator. Hence, the filter update strategy has been slightly modified not to be updated when the speed of the vehicle is below $30kph\,(\approx 8.3m/s)$.

Fig. 24 shows the geometrical parameter identification results in the road test. The identification of vehicle CoG location stabilized with the estimated value of $1.48m$ with $0.15m$ 1-sigma boundary, while the previous result with $-0.4m$ sensor lever-arm converged into $1.38m$, and the corresponding error from measured CoG position, $1.44m$, are $0.04m\,(2.78\%)$ and $-0.06m\,(4.17\%)$ respectively, which can be considered in the typical varying range with occupants, fuel, or luggage. The sensor lever-arm identification results in $0.22m$ for the last 100 seconds of data, while the actual value is measured to be $0.25m$ forward from vehicle CoG.

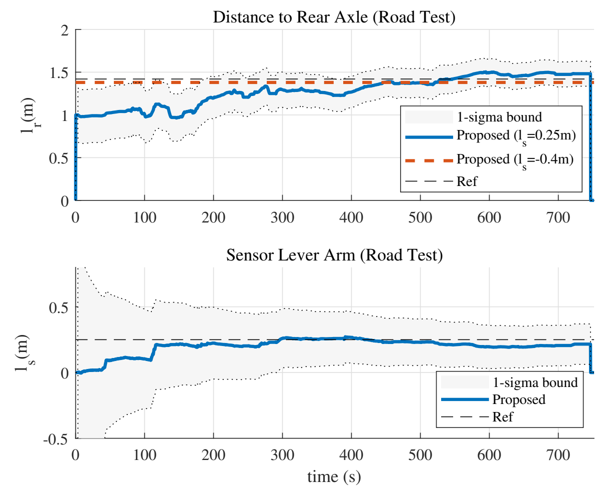

Fig. 24. Geometrical parameter identification results in Road Test. Blue line shows the identification results with 0.25m sensor lever arm and red-dotted line is for the identification result from previous section with -0.4m sensor lever-arm. (top) Vehicle CoG position identification (bottom) Sensor lever-arm identification

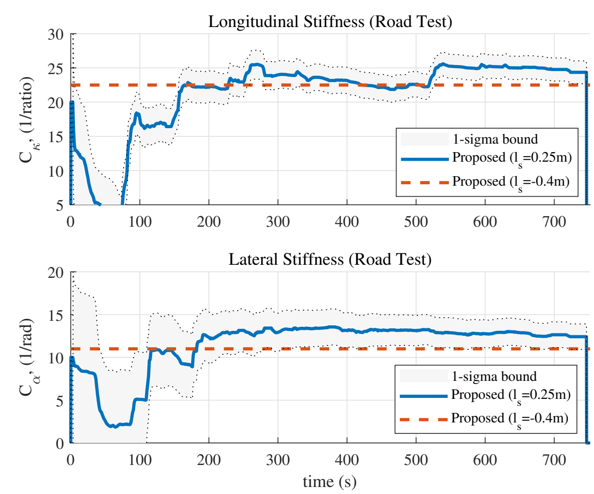

Fig. 25. Tire stiffness identification results in Road Test. Blue line shows the identification results with 0.25m sensor lever arm and red-dotted line is for the identification results from previous section with -0.4m sensor lever-arm. (top) Longitudinal tire stiffness (bottom) Lateral tire stiffness

The tire stiffness identification results for the road test scenario are given in Fig. 25. Compared with the previous experimental results, both longitudinal and lateral stiffness result in somewhat higher value: The identified stiffness for the last 100 seconds of estimation results in 24.3 for longitudinal and 12.4 for lateral, while the previous experiment had 22.6 and 11.2, which are 7% and 9.7% in errors, respectively. The errors are considered in the reasonable range to be applied in state estimations or control applications referring to the related works [51], [52], factoring in that those tests are taken in the different roads.

V. Conclusion

This paper addresses a novel vehicle dynamics and sensor lever-arm identification method for in-vehicle mounted motion sensing devices. We proposed a modified single track model in consideration of the measurement lever-arm with normalized tire stiffness to solve the circular dependency on vehicle model identification and lever-arm estimation. The inertial and pose estimation result fused with the modified single track model via UKF to establish an in-run identification of the parameter set. The proposed identification method was demonstrated both in simulation and real-vehicle experiments with promising results. We hope that the proposed identification method facilitates researchers in related fields that conjugate vehicle dynamics with modern techniques for localization and pose estimation from various sensing domains.

Furthermore, we intend to adopt the brushed tire model to expand the dynamics coverage of the proposed methods toward the nonlinear region of force-slip curves. Also, a design of parallel estimation of vehicle states and model parameters would be seen in our future framework for the unified vehicle state estimation with multi-modality of external sensing devices.

References

[1] V. K. Kukkala, J. Tunnell, S. Pasricha, and T. Bradley, "Advanced driver-assistance systems: A path toward autonomous vehicles," *IEEE Consumer Electronics Magazine*, vol. 7, no. 5, pp. 18–25, 2018.

[2] E. Abbott and D. Powell, "Land-vehicle navigation using gps," *Proceedings of the IEEE*, vol. 87, no. 1, pp. 145–162, 1999.

[3] Z. Li, J. Wang, B. Li, J. Gao, and X. Tan, "Gps/ins/odometer integrated system using fuzzy neural network for land vehicle navigation applications," *The Journal of Navigation*, vol. 67, no. 6, pp. 967–983, 2014.

[4] X. Niu, S. Nassar, and N. EL-SHEIMY, "An accurate land-vehicle mems imu/gps navigation system using 3d auxiliary velocity updates," *Navigation*, vol. 54, no. 3, pp. 177–188, 2007.

[5] Q. C. Sun, J. C. Xia, J. Foster, T. Falkmer, and H. Lee, "Pursuing precise vehicle movement trajectory in urban residential area using multi-gnss rtk tracking," *Transportation research procedia*, vol. 25, pp. 2356–2372, 2017.

[6] M. Higuchi and N. Kubo, "Achievement of continuous decimeter-level accuracy using low-cost single-frequency receivers in urban environments," in *Proceedings of the 29th International Technical Meeting of the Satellite Division of the Institute of Navigation (ION GNSS+ 2016)*, pp. 1891–1913, 2016.

[7] D. Nistér, O. Naroditsky, and J. Bergen, "Visual odometry," in *Proceedings of the 2004 IEEE Computer Society Conference on Computer Vision and Pattern Recognition, 2004. CVPR 2004.*, vol. 1, pp. I–I, Ieee, 2004.

[8] D. Nistér, O. Naroditsky, and J. Bergen, "Visual odometry for ground vehicle applications," *Journal of Field Robotics*, vol. 23, no. 1, pp. 3–20, 2006.

[9] L. Von Stumberg, V. Usenko, and D. Cremers, "Direct sparse visual-inertial odometry using dynamic marginalization," in *2018 IEEE International Conference on Robotics and Automation (ICRA)*, pp. 2510–2517, IEEE, 2018.

[10] T. Qin, P. Li, and S. Shen, "Vins-mono: A robust and versatile monocular visual-inertial state estimator," *IEEE Transactions on Robotics*, vol. 34, no. 4, pp. 1004–1020, 2018.

[11] J. Zhang and S. Singh, "Loam: Lidar odometry and mapping in real-time.," in *Robotics: Science and Systems*, vol. 2, 2014.

[12] Y. Almalioglu, M. Turan, C. X. Lu, N. Trigoni, and A. Markham, "Milli-rio: Ego-motion estimation with low-cost millimetre-wave radar," *IEEE Sensors Journal*, vol. 21, no. 3, pp. 3314–3323, 2020.

[13] S. H. Cen and P. Newman, "Precise ego-motion estimation with millimeter-wave radar under diverse and challenging conditions," in *2018 IEEE International Conference on Robotics and Automation (ICRA)*, pp. 6045–6052, IEEE, 2018.

[14] G. Park, S. B. Choi, D. Hyun, and J. Lee, "Integrated observer approach using in-vehicle sensors and gps for vehicle state estimation," *Mechatronics*, vol. 50, pp. 134–147, 2018.

[15] D. M. Bevly, J. C. Gerdes, C. Wilson, and G. Zhang, "The use of gps based velocity measurements for improved vehicle state estimation," in *Proceedings of the 2000 American Control Conference. ACC (IEEE Cat. No. 00CH36334)*, vol. 4, pp. 2538–2542, IEEE, 2000.

[16] V. Rodrigo Marco, J. Kalkkuhl, J. Raisch, and T. Seel, "A novel imu extrinsic calibration method for mass production land vehicles," *Sensors*, vol. 21, no. 1, p. 7, 2021.

[17] R. Kang, L. Xiong, M. Xu, J. Zhao, and P. Zhang, "Vins-vehicle: A tightly-coupled vehicle dynamics extension to visual-inertial state estimator," in *2019 IEEE Intelligent Transportation Systems Conference (ITSC)*, pp. 3593–3600, IEEE, 2019.

[18] J. Jeon, Y. Hwang, Y. Jeong, S. Park, I. S. Kweon, and S. B. Choi, "Lane detection aided online dead reckoning for gnss denied environments," *Sensors*, vol. 21, no. 20, p. 6805, 2021.

[19] M. Fazekas, P. Gáspár, and B. Németh, "Vision-based motion estimation for vehicles on test track via cone markers," in *2020 11th IEEE International Conference on Cognitive Infocommunications (CogInfoCom)*, pp. 000387–000392, IEEE, 2020.

[20] W. Liu, L. Xiong, X. Xia, Y. Lu, L. Gao, and S. Song, "Vision-aided intelligent vehicle sideslip angle estimation based on a dynamic model," *IET Intelligent Transport Systems*, vol. 14, no. 10, pp. 1183–1189, 2020.

[21] A. Wischnewski, T. Stahl, J. Betz, and B. Lohmann, "Vehicle dynamics state estimation and localization for high performance race cars," *IFAC-PapersOnLine*, vol. 52, no. 8, pp. 154–161, 2019.

[22] Q. Zhang, Y. Hu, and X. Niu, "Required lever arm accuracy of non-holonomic constraint for land vehicle navigation," *IEEE Transactions on Vehicular Technology*, vol. 69, no. 8, pp. 8305–8316, 2020.

[23] Y. Wu, M. Wu, X. Hu, and D. Hu, "Self-calibration for land navigation using inertial sensors and odometer: Observability analysis," in *AIAA Guidance, Navigation, and Control Conference*, p. 5970, 2009.

[24] Q. Chen, Q. Zhang, and X. Niu, "Estimate the pitch and heading mounting angles of the imu for land vehicular gnss/ins integrated system," *IEEE transactions on intelligent transportation systems*, 2020.

[25] Q. Zhang, Y. Hu, S. Li, T. Zhang, and X. Niu, "Mounting parameter estimation from velocity vector observations for land vehicle navigation," *IEEE Transactions on Industrial Electronics*, 2021.

[26] K. I. S. C. S. Hwang Yoonjin, Jeong Yongseop, "Online misalignment estimation of strapdown navigation for land vehicle under dynamic condition," *International Journal of Automotive Technology*, vol. 22, no. 6, pp. 1723–1733, 2021.

[27] M. Viehweger, C. Vaseur, S. van Aalst, M. Acosta, E. Regolin, A. Alatorre, W. Desmet, F. Naets, V. Ivanov, A. Ferrara, *et al.*, "Vehicle state and tyre force estimation: demonstrations and guidelines," *Vehicle system dynamics*, vol. 59, no. 5, pp. 675–702, 2021.

[28] J. Lee, D. Hyun, K. Han, and S. Choi, "Real-time longitudinal location estimation of vehicle center of gravity," *International Journal of Automotive Technology*, vol. 19, no. 4, pp. 651–658, 2018.

[29] S. L. Miller, B. Youngberg, A. Millie, P. Schweizer, and J. C. Gerdes, "Calculating longitudinal wheel slip and tire parameters using gps velocity," in *Proceedings of the 2001 American Control Conference.(Cat. No. 01CH37148)*, vol. 3, pp. 1800–1805, IEEE, 2001.

[30] D. M. Bevly, R. Sheridan, and J. C. Gerdes, "Integrating ins sensors with gps velocity measurements for continuous estimation of vehicle sideslip and tire cornering stiffness," in *Proceedings of the 2001 American Control Conference.(Cat. No. 01CH37148)*, vol. 1, pp. 25–30, IEEE, 2001.

[31] G. Baffet, A. Charara, and D. Lechner, "Estimation of vehicle sideslip, tire force and wheel cornering stiffness," *Control Engineering Practice*, vol. 17, no. 11, pp. 1255–1264, 2009.

[32] G. Reina, M. Paiano, and J.-L. Blanco-Claraco, "Vehicle parameter estimation using a model-based estimator," *Mechanical Systems and Signal Processing*, vol. 87, pp. 227–241, 2017.

[33] K. Han, M. Choi, and S. B. Choi, "Estimation of the tire cornering stiffness as a road surface classification indicator using understeering characteristics," *IEEE Transactions on Vehicular Technology*, vol. 67, no. 8, pp. 6851–6860, 2018.

[34] M. C. Best, A. P. Newton, and S. Tuplin, "The identifying extended kalman filter: parametric system identification of a vehicle handling model," *Proceedings of the Institution of Mechanical Engineers, Part K: Journal of Multi-body Dynamics*, vol. 221, no. 1, pp. 87–98, 2007.

[35] C. Lundquist and T. B. Schön, "Recursive identification of cornering stiffness parameters for an enhanced single track model," *IFAC Proceedings Volumes*, vol. 42, no. 10, pp. 1726–1731, 2009.

[36] D. Wesemeier and R. Isermann, "Identification of vehicle parameters using stationary driving maneuvers," *Control engineering practice*, vol. 17, no. 12, pp. 1426–1431, 2009.
[37] T. Wenzel, K. Burnham, M. Blundell, and R. Williams, "Kalman filter as a virtual sensor: applied to automotive stability systems," *Transactions of the Institute of Measurement and Control*, vol. 29, no. 2, pp. 95–115, 2007.
[38] T. A. Wenzel, K. Burnham, M. Blundell, and R. Williams, "Dual extended kalman filter for vehicle state and parameter estimation," *Vehicle system dynamics*, vol. 44, no. 2, pp. 153–171, 2006.
[39] J. Domhof, J. F. P. Kooij, and D. M. Gavrila, "A joint extrinsic calibration tool for radar, camera and lidar," *IEEE Transactions on Intelligent Vehicles*, vol. 6, no. 3, pp. 571–582, 2021.
[40] Z. Liu, L. Wang, F. Wen, and H. Zhang, "Imu/vehicle calibration and integrated localization for autonomous driving," in *2021 IEEE International Conference on Robotics and Automation (ICRA)*, pp. 4013–4019, IEEE, 2021.
[41] S. J. Julier, J. K. Uhlmann, and H. F. Durrant-Whyte, "A new approach for filtering nonlinear systems," in *Proceedings of 1995 American Control Conference-ACC'95*, vol. 3, pp. 1628–1632, IEEE, 1995.
[42] S. J. Julier and J. K. Uhlmann, "New extension of the kalman filter to nonlinear systems," in *Signal processing, sensor fusion, and target recognition VI*, vol. 3068, pp. 182–193, International Society for Optics and Photonics, 1997.
[43] E. Tunali and T.-J. Tarn, "New results for identifiability of nonlinear systems," *IEEE Transactions on Automatic Control*, vol. 32, no. 2, pp. 146–154, 1987.
[44] A. F. Villaverde, N. Tsiantis, and J. R. Banga, "Full observability and estimation of unknown inputs, states and parameters of nonlinear biological models," *Journal of the Royal Society Interface*, vol. 16, no. 156, p. 20190043, 2019.
[45] J. Karlsson, M. Anguelova, and M. Jirstrand, "An efficient method for structural identifiability analysis of large dynamic systems," *IFAC proceedings volumes*, vol. 45, no. 16, pp. 941–946, 2012.
[46] J. Rehder, J. Nikolic, T. Schneider, T. Hinzmann, and R. Siegwart, "Extending kalibr: Calibrating the extrinsics of multiple imus and of individual axes," in *2016 IEEE International Conference on Robotics and Automation (ICRA)*, pp. 4304–4311, IEEE, 2016.
[47] S. G. Klauer, T. A. Dingus, V. L. Neale, J. D. Sudweeks, and D. J. Ramsey, "Comparing real-world behaviors of drivers with high versus low rates of crashes and near crashes," tech. rep., 2009.
[48] U. Kiencke and L. Nielsen, "Automotive control systems: for engine, driveline, and vehicle," 2000.
[49] H. B. Pacejka and R. S. Sharp, "Shear force development by pneumatic tyres in steady state conditions: a review of modelling aspects," *Vehicle system dynamics*, vol. 20, no. 3-4, pp. 121–175, 1991.
[50] M. K. Salaani, "Analytical tire forces and moments model with validated data," *SAE Transactions*, pp. 735–763, 2007.
[51] K. B. Singh and S. Taheri, "Estimation of tire–road friction coefficient and its application in chassis control systems," *Systems Science & Control Engineering*, vol. 3, no. 1, pp. 39–61, 2015.
[52] K. Berntorp and S. Di Cairano, "Tire-stiffness and vehicle-state estimation based on noise-adaptive particle filtering," *IEEE Transactions on Control Systems Technology*, vol. 27, no. 3, pp. 1100–1114, 2018.

Yoonjin Hwang received the B.S. degree in physics and mechanical engineering from Sogang University, Seoul, South Korea, in 2013 and the M.S. degree in mechanical engineering from Korea Advanced Institute of Science and Technology(KAIST), Daejeon, South Korea in 2015, where he is currently working toward the Ph.D. degree.

From 2016, He is co-founder of 3Secondz Inc., which is a startup supplying driving data acquisition and automated report generation platform. His research interests include sensor fusion for localization and state estimation, vehicle dynamics, and autonomous vehicles.

Yongseop Jeong received the B.S. degree in Electrical and Computer Engineering from Sungkyunkwan University, Seoul, South Korea, in 2011 and the M.S. degree in Robotics Program from Korea Advanced Institute of Science and Technology(KAIST), Daejeon, South Korea in 2013, where he is currently working toward the Ph.D. degree.

His research interests include sensor fusion, system integration for perception of autonomous vehicles.

In So Kweon received the B.S. and the M.S. degrees in Mechanical Design and Production Engineering from Seoul National University, Korea, in 1981 and 1983, respectively, and the Ph.D. degree in Robotics from the Robotics Institute at Carnegie Mellon University in 1990.

He worked for Toshiba R&D Center, Japan, and joined KAIST in 1992. He is KEPCO endowed chair professor of electrical engineering (EE) and the director for the National Core Research Center – P3 DigiCar Center at KAIST.

Professor Kweon's research interests include computer vision and robotics. He has co-authored several books, including "Metric Invariants for Camera Calibration," and more than 300 technical papers. He served as a Founding Associate-Editor-in-Chief for "International Journal of Computer Vision and Applications", and has been an Editorial Board Member for "International Journal of Computer Vision" since 2005.

Seibum B. Choi (M'09) received the B.S. degree in mechanical engineering from Seoul National University, Seoul, Korea in 1985, the M.S. degree in mechanical engineering from the Korea Advanced Institute of Science and Technology(KAIST), Daejeon, South Korea, in 1987, and the Ph.D. degree in control from the University of California, Berkeley, CA, USA, in 1993.

From 1993 to 1997, he was involved in the development of automated vehicle control systems at the Institute of Transportation Studies, University of California. In 2006, he was with TRW, Warren, MI, USA, where he was involved in the development of advanced vehicle control systems. Since 2006, he has been with the faculty of the Department of Mechanical Engineering, KAIST. His current research interets include fuel-saving technologies, vehicle dynamics and control, and active safety systems.